

Smooth Shells: Multi-Scale Shape Registration with Functional Maps

MARVIN EISENBERGER, Technical University of Munich, Germany

ZORAH LÄHNER, Technical University of Munich, Germany

DANIEL CREMERS, Technical University of Munich, Germany



Fig. 1. Given a source (left) and target (right) shape we propose a hierarchical smoothing procedure to iteratively align the inputs. We alternate between aligning our smooth shells and computing the correspondences which we represent using Functional Maps [32]. The combination of extrinsic and intrinsic information in combination with the coarse-to-fine strategy allows for a registration of challenging interclass registration tasks like morphing a dog to a horse. In the end we can apply the morphing to the source shape to get an alignment for the two inputs.

We propose a novel 3D shape correspondence method based on the iterative alignment of so-called smooth shells. Smooth shells define a series of coarse-to-fine, smooth shape approximations that are designed to work well with multiscale algorithms. In this paper, we alternate between aligning smooth shells and computing Functional Maps between the inputs. Aligning very smooth approximations reduces the complexity of the overall process but during the iterations the amount of detail in the shells increases which helps to refine the resulting correspondence. Furthermore, we solve the problem of ambiguities from intrinsic symmetries by applying a surrogate based Markov chain Monte Carlo initialization. We show state-of-the-art quantitative results on several datasets focussing on isometries, topological changes and different connectivity. Additionally, we show qualitative results on challenging interclass pairs.

ACM Reference Format:

Marvin Eisenberger, Zorah Löhner, and Daniel Cremers. 2024. Smooth Shells: Multi-Scale Shape Registration with Functional Maps. 1, 1 (December 2024), 11 pages. <https://doi.org/10.1145/nnnnnnn.nnnnnnn>

1 INTRODUCTION

The wide selection of affordable 3D scanning devices in recent years has led to an enormous growth of the amount of 3D shapes and scans available. In contrast to artificially created shapes, certain properties cannot be guaranteed by real-world scans. For example, topological noise might appear in self-touching areas or the meshing density

Authors' addresses: Marvin Eisenberger, Technical University of Munich, Boltzmannstrasse 3, Garching, 85748, Germany, marvin.eisenberger@in.tum.de; Zorah Löhner, Technical University of Munich, Boltzmannstrasse 3, Garching, 85748, Germany, laehner@in.tum.de; Daniel Cremers, Technical University of Munich, Boltzmannstrasse 3, Garching, 85748, Germany, cremers@tum.de.

Permission to make digital or hard copies of all or part of this work for personal or classroom use is granted without fee provided that copies are not made or distributed for profit or commercial advantage and that copies bear this notice and the full citation on the first page. Copyrights for components of this work owned by others than ACM must be honored. Abstracting with credit is permitted. To copy otherwise, or republish, to post on servers or to redistribute to lists, requires prior specific permission and/or a fee. Request permissions from permissions@acm.org.

© 2024 Association for Computing Machinery.

XXXX-XXXX/2024/12-ART \$15.00

<https://doi.org/10.1145/nnnnnnn.nnnnnnn>

can vary between different areas and instances of the same shape. These distortions have been shown to be difficult for current shape correspondence methods [21, 29]. Traditional methods focus only on the (nearly) isometric case or clearly defined extensions of this, for example partiality [25]. Another approach is to learn how to produce correspondences between different classes of shapes or under certain perturbations [17]. Unfortunately, this requires training data and knowledge about what deformations and noise are to be expected.

One can distinguish between intrinsic and extrinsic methods. Intrinsic methods are based on properties only derived from surface properties that are independent of the embedding, for example the Laplace-Beltrami operator. While they can cope with topological changes, they often provide suboptimal correspondence results in the presence of extreme pose changes. On the other hand, extrinsic methods use the information of the embedding space which makes extreme pose changes challenging but not topological changes. A natural step would be to combine both in order to attain the best of both worlds. A few attempts have been made in this direction [11, 14] and we aim to continue this line of work.

In this paper, we aim at combining intrinsic and extrinsic knowledge by using Functional Maps to represent correspondences but enrich this information by additionally aligning the inputs in the embedding space. For this purpose, we define so-called smooth shells that allow us to approach this problem in a coarse-to-fine matter and show that this leads to a highly flexible framework that can solve for meaningful correspondences beyond the isometry assumption and in the presence of different types of noise.

1.1 Contribution

We propose a coarse-to-fine approach to shape registration. The main idea is to iteratively align smooth shells which are smoothed approximations of the input shapes. During the iterations more details and pose refinements are added. Due to a special property of our smooth shells each iteration only has to deal with minor changes in the geometry. Like this we alternate between computing the shell

alignment and the correspondences between the two surfaces. We represent the surface correspondences with Functional Maps [32] which allows for a compact representation with exactly the right level of detail for our shells. Additionally, we propose a Markov chain Monte Carlo initialization strategy to disambiguate self similarities of input shapes and prevent our method from getting stuck in local minima. The combination of Functional Maps with extrinsic morphing creates state-of-the-art results on established datasets and challenging examples.

2 RELATED WORK

2.1 Shape Correspondence and Registration

Shape correspondence is an extensive topic in literature and surveys of state-of-the-art methods [42, 46, 49] give a broader overview of existing approaches. In this section, we will focus on work immediately related to ours.

Functional Maps [32] are often used in applications that require correspondences between shapes and have been extended to work for many applications [26, 36, 39]. One of the main advantages is the dimensionality reduction of the correspondence problem which allows for efficient optimization and representation. More complicated is the task of extracting a point-wise correspondence from a Functional Map [40]. Due to being purely intrinsic Functional Maps often struggle with self-symmetries and the low-frequency representation leads to locally inaccurate solutions. There are several methods which tackle this problem but most of them are computationally heavy [31, 36, 40] or make restrictive underlying assumptions about properties of the inputs [51]. A notable exception from this is [16].

Other directions include calculating a deformation field to align the input surfaces with each other. [27, 30] also model the mapping from a surface to the embedding space with a low rank basis. Like our approach, [15] alternates between calculating a deformation field and correspondences but the volume-preservation constraint restricts the applicability. Many deformation-based methods require expensive preprocessing of the inputs to apply the deformation model, for example with a deformation graph [43], structural rods [3] or deep learning [17]. Instead of a deformation field ICP-based method iteratively move the vertices until the inputs align well. Non-rigid ICP variations can register shapes in different poses and classes but rely on a good initialization [4, 23]. When the shapes undergo too serve deformation it might even be impossible to find a initialization that is close enough too work.

There exist very accurate methods to register certain classes of shapes, especially humans [7]. Unfortunately, these are highly specialized and depend on class specific features [28] or learning statistical models from data [35]. While these methods exceed within their classes, they can not be applied to new data like our framework can.

2.2 Shape Approximation and Simplification

The idea of mesh simplification by smoothing was investigated thoroughly in previous work. E.g. [48] use manifold harmonics for the smoothing. In surface deformation modeling this is usually a two stage algorithm. First, a smoothed version of a shape is deformed and then the details are added back to the surface, see [8] for an overview. Some classical works on shape modeling with smoothing

are [18] and [20]. [9] combines this approach with differential coordinates. Although our smooth shells are closely related, especially to [48], none of the mentioned approaches offers a series of approximations with guaranteed small geometry variation between consecutive elements.

Another way to simply shapes is via skeletons. Skeletons of shapes form a lower-dimensional and compact description of the overall shape and are used in many Computer Graphics applications. A recent survey of 3D skeleton methods can be found in [45]. Although the skeletons are often designed to be easily aligned between different shapes and similar classes, they are designed to create a single, unique skeleton for each shape. This is useful for a rough alignment but does not allow an iterative refinement of the surface alignment as is needed in our method. Similar to our method, [13] extracts a skeleton based on Laplacian-based contraction but aims at getting a unique curve skeleton. Some methods exist to create an entire class of skeletons for each shape [37]. Our method differs from the previously mentioned in that we do not introduce a fixed skeleton for each shape but use a class of approximations with increasing level of details.

3 BACKGROUND

The problem instances we consider consist of two input shapes \mathcal{X} and \mathcal{Y} . We assume any shapes \mathcal{X} (or \mathcal{Y}) are 2D Riemannian manifolds embedded in 3D with their coordinate function denoted by $X : \mathcal{X} \rightarrow \mathbb{R}^3$. In particular, \mathcal{X} is equipped with a smooth inner product $\langle f, g \rangle = \int_{\mathcal{X}} f(x) \cdot g(x) dx$ on the surface where dx denotes the area element on \mathcal{X} . Furthermore, we consider the space of L^2 integrable functions on \mathcal{X} denoted as $\mathcal{F}(\mathcal{X}) = \{f : \mathcal{X} \rightarrow \mathbb{R} \mid \|f\|^2 = \langle f, f \rangle < \infty\}$.

The general problem setup that is typically investigated for a pair of shapes is shape correspondence which aims at finding a mapping $\mathbf{P} : \mathcal{X} \rightarrow \mathcal{Y}$ that associates points $p \in \mathcal{X}$ with meaningful counterparts on \mathcal{Y} . However, in this paper we look at the more general problem of shape registration where apart from the surface-to-surface mapping we also determine a surface to \mathbb{R}^3 mapping morphing the shape \mathcal{X} . This then results in a morphed shape $\hat{\mathcal{X}}$ from which we can compute \mathbf{P} with a nearest neighbor search in some appropriate embedding space.

3.1 Laplace-Beltrami Operator

The Laplace-Beltrami operator $\Delta^{\mathcal{X}}$ on a manifold \mathcal{X} is an extension of the standard Euclidean Laplace operator to manifold domains and defined such that $\Delta^{\mathcal{X}} f = \text{div}(\nabla f)$ for any function f defined on the surface of \mathcal{X} . Computing solutions of the corresponding eigenproblem $\Delta^{\mathcal{X}} \phi_k = \lambda_k^{\mathcal{X}} \phi_k$ yields the Laplace-Beltrami eigenpairs $(\phi_k, \lambda_k^{\mathcal{X}})$ with $\dots \leq \lambda_2^{\mathcal{X}} < \lambda_1^{\mathcal{X}} = 0$. The set of eigenfunctions $\{\phi_k\}_{k \in \mathbb{N}}$ form an orthonormal basis of $\mathcal{F}(\mathcal{X})$ wrt. the inner product $\langle \cdot, \cdot \rangle$. Furthermore, the eigenfunctions ϕ_k are naturally ordered from low to high frequency using the order of eigenvalues. Therefore, a truncated sum projecting on the first K eigenfunctions ϕ_1, \dots, ϕ_K gives a low-frequency approximation that, according to the min-max principle is optimal for smooth functions $f \in \mathcal{F}(\mathcal{X})$ [33].

$$f \approx \tilde{f} = \sum_{k=1}^K \underbrace{\langle f, \phi_k \rangle}_{\hat{f}_k} \phi_k. \quad (1)$$

In this paper we call $\hat{f}_k = (\hat{f}_k)_k$ the truncated Fourier coefficients of f and $\mathcal{T}_K : \mathcal{F}(\mathcal{X}) \rightarrow \mathcal{F}(\mathcal{X})$ the projection operator of $f \mapsto \tilde{f} = \mathcal{T}_K f$ truncating the spectral coefficients $k > K$.

$$\mathcal{T}_K := \sum_{k=1}^K \phi_k \otimes \phi_k. \quad (2)$$

The the projection operator of f on the ϕ_k can be written as the outer product $\phi_k \otimes \phi_k$.

3.2 Discretization

We use triangle meshes to represent the Riemannian manifolds \mathcal{X} and \mathcal{Y} with N and M points respectively. We denote the coordinate matrices as $X \in \mathbb{R}^{N \times 3}$ and $Y \in \mathbb{R}^{M \times 3}$ and individual points as $x_i, y_i \in \mathbb{R}^3$. The inner product of two functions $f, g \in \mathbb{R}^N$ can be discretized as $\langle f, g \rangle = \sum_{n=1}^N f_n \cdot g_n \cdot dx_n$ where $dx_n > 0$ are the discrete area elements at each point. Furthermore, we use the standard cotangent discretization of the Laplace-Beltrami operator $\Delta^{\mathcal{X}} \in \mathbb{R}^{N \times N}$ with lumped mass matrix and denote its eigenvectors as $\phi_1, \dots, \phi_N \in \mathbb{R}^N$ [34]. For \mathcal{Y} we call the eigenvectors $\psi_1, \dots, \psi_M \in \mathbb{R}^M$.

3.3 Functional Maps

The Functional Map framework [32] is a popular approach to solve for a shape correspondence $\mathbf{P} : \mathcal{X} \rightarrow \mathcal{Y}$. The main idea is to replace \mathbf{P} with a mapping of functions to functions $\mathbf{C} : \mathcal{F}(\mathcal{X}) \rightarrow \mathcal{F}(\mathcal{Y})$. This functional \mathbf{C} is linear and can be represented in matrix form using its spectral decomposition.

$$\mathbf{C}f = \sum_{l=1}^{\infty} \langle \mathbf{C}f, \psi_l \rangle \psi_l = \sum_{k,l=1}^{\infty} \underbrace{\langle \mathbf{C}\phi_k, \psi_l \rangle}_{c_{kl}} \langle f, \phi_k \rangle \psi_l. \quad (3)$$

Using Equation (1) the approximate Functional Map can be written as the matrix $\mathbf{C} = (c_{kl})_{k,l} \in \mathbb{R}^{K \times K}$ transforming the spectral coefficients \hat{f} of f to those of the mapped function $\hat{g} = \mathbf{C}\hat{f}$.

If we assume that the mapping \mathbf{P} is area preserving, we can restrict ourselves to orthonormal Functional Maps $\mathbf{C}^T \mathbf{C} = \mathbf{I}$, see [32, Theorem 5.1]. For pairs of functions $f_i : \mathcal{X} \rightarrow \mathbb{R}$ and $g_i : \mathcal{Y} \rightarrow \mathbb{R}$ that are known to describe the same properties on both shapes, for example descriptor functions or landmarks, \mathbf{C} can be determined by solving the following Procrustes problem.

$$\mathbf{C} = \arg \min_{\mathbf{C}^T \mathbf{C} = \mathbf{I}} \|\mathbf{C}\hat{\mathbf{F}} - \hat{\mathbf{G}}\|_F. \quad (4)$$

$\hat{\mathbf{F}}$ and $\hat{\mathbf{G}}$ are the matrices of the stacked spectral coefficients $\hat{f}_i, \hat{g}_i \in \mathbb{R}^K$ of f_i and g_i .

Throughout this paper it becomes clear that functional correspondences are the most natural way to encode similarities between our smooth shells because they are themselves represented in a spectral basis of the same dimension. Like this we merely use Functional Maps as a tool to encode similarities between our shells but do not entirely rely on intrinsic information.

4 METHOD

We propose to solve shape correspondence by iteratively aligning a series of coarse-to-fine approximations of two input manifolds \mathcal{X} and \mathcal{Y} . Our algorithm alternates between

- (1) solving for a pointwise correspondence using Functional Maps and

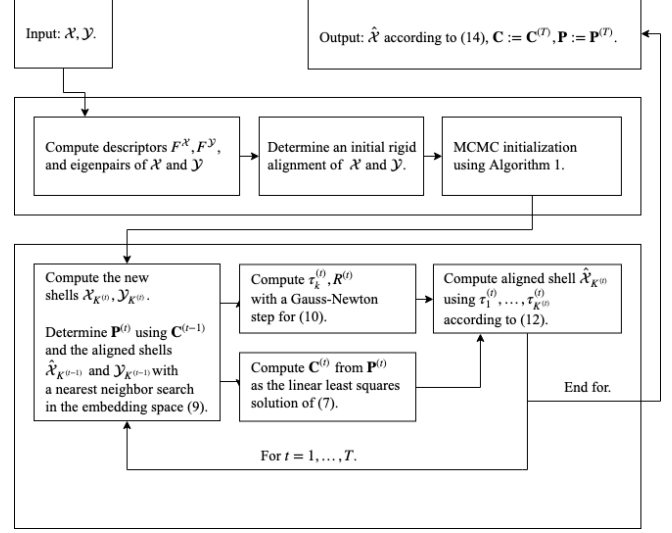


Fig. 2. The figure above displays the main steps in our registration pipeline. Details for the individual steps are provided in the respective subsections of Chapter 4.

- (2) aligning so-called smooth shells that hierarchically approximate the input shapes

The algorithm is based on the idea that the alignment of two coarse shapes is easier without the distraction of small scale features while those are highly useful for the exact alignment in the end. The smooth shells we use as approximations are introduced in Section 4.1. Section 4.2 explains the correspondence computation and Section 4.3 the alignment step. See Figure 2 for an overview of the complete pipeline and see Figure 4 for an example of how our method hierarchically aligns shells for a pair of input shapes.

For the rest of the paper we will reference the iterations by numbering them with $t = 0, \dots, T$. Each iteration has a corresponding smoothing parameter $K^{(t)}$ such that $K^{(t)} < K^{(t+1)}$ and the corresponding smooth shells $(\mathcal{X}_{K^{(t)}})_{t=0, \dots, T}$ and $(\mathcal{Y}_{K^{(t)}})_{t=0, \dots, T}$. We drop (t) if it is clear from context.

For the first iteration, when there is no initialization from the previous iteration, we incorporate a surrogate based initialization strategy to compute an initial alignment of the coarse shells. This strategy also avoids mixing self-similarities like intrinsic symmetries which are easily mistaken already in the initial state. See Section 5 for details.

4.1 Smooth Shells

Our definition of smooth shells is similar to the one of spectral reconstruction [22] but we extended it to suit the task of iterative alignment better. Both can be parametrized with a parameter K that indicates how many details should be preserved. A small K leads to very smoothed out geometry while higher K generate more and more details.

4.1.1 Spectral Reconstruction. Spectral reconstruction [22] works by projecting the x -, y - and z -coordinate functions of \mathcal{X} onto the first

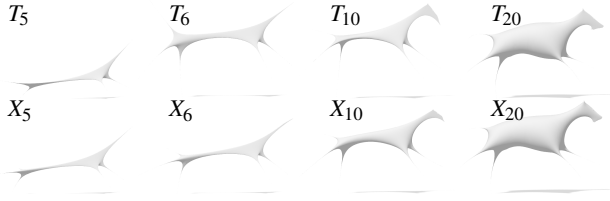


Fig. 3. Examples of different T_K and $X_K := S_K(X)$ on a running dog. Notice how the difference in height between T_5 and T_6 is changing whereas X_5 and X_6 are very similar. For higher K the shapes become more similar.

K eigenfunctions of the Laplace-Beltrami operator.

$$T_K := (\mathcal{T}_K(x), \mathcal{T}_K(y), \mathcal{T}_K(z)) = \sum_{k=1}^K \langle (x, y, z), \phi_k \rangle \phi_k. \quad (5)$$

$\langle \cdot, \cdot \rangle : \mathcal{F}(X)^3 \times \mathcal{F}(X) \rightarrow \mathbb{R}^3$ is with a slight abuse of notation the vector of elementwise inner products of the three components. Since the eigenfunctions are ordered by frequency this creates an approximation of the original shape, showing only the global structure if $K \approx 10$ but becoming more detailed as K increases. Figure 3 illustrates this coarse-to-fine approximation for multiple K . For $K \rightarrow \infty$ the shapes X_K converge to the original shape X but in practice a couple of hundred eigenfunctions are sufficient to approximate X faithfully.

Remark. A well-known property of the Laplace-Beltrami eigenfunctions ϕ_k is that they encode the geometry of X from low to high frequency structures. Especially the first eigenfunctions have a nice direct geometric interpretation for many examples. For instance, the first eigenfunction is constant and therefore \mathcal{T}_1 projects the whole shape on one point at the mean coordinates. \mathcal{T}_2 maps the geometry to a straight line that constitutes the main axis of the shape. The next few eigenfunctions $K \geq 3$ correspond to global features of X like limbs or other extremities. Finally, the higher order eigenfunctions $K \geq 100$ locate small scale features like details in the face.

4.1.2 Shell Operator. We introduce the *shell operator* S_K as a variation of the spectral reconstruction that is better suited for iterative alignment.

$$S_K := \sum_{k=1}^{\infty} \frac{1}{1 + \exp(\sigma(k - K))} \phi_k \otimes \phi_k. \quad (6)$$

This operator consists of a weighted series of projections on the eigenfunctions ϕ_k . The sigmoid weights we propose are close to 1 if $k \ll K$ and decay to 0 when $k \gg K$. This smooths the shape but guarantees that the difference in geometry between S_K and S_{K+1} is not too severe for small σ . For $\sigma \rightarrow \infty$ the sigmoid weighting function converges to the indicator function $\mathbf{1}_{\{k \leq K\}}$ almost everywhere which corresponds to the truncation of the spectrum in \mathcal{T}_K . See Figure 3 for the difference between \mathcal{T}_K and S_K .

Remark. The truncated coordinates from the operator \mathcal{T}_K are not well suited for our pipeline because we are interested in iteratively aligning $\mathcal{T}_K(X)$ with $\mathcal{T}_K(Y)$. Two undesirable effects can occur when using \mathcal{T}_K . First, for small K the difference in geometry between $\mathcal{T}_K(X)$ and $\mathcal{T}_{K+1}(X)$ can be rather severe, for example adding an entire extremity that was not there before. This leads to unstable behavior when initializing with the result of the previous iteration.

Second, for non-isometric shapes the order of eigenfunctions might not represent the same geometry, introducing errors when aligning $\mathcal{T}_K(X)$ and $\mathcal{T}_K(Y)$. Even for nearly isometric pairs small deviations and intrinsic symmetries (i.e. two eigenvalues of the same magnitude) might swap the ordering of some eigenfunctions. In this case, the eigenfunctions ϕ_K^X and ϕ_K^Y can encode completely different parts of the shapes and the shapes with truncated coordinates $\mathcal{T}_K(X)$ and $\mathcal{T}_K(Y)$ cannot be aligned in a meaningful way.

Our smoothing operator S_K can now be applied to the input shape coordinate function X which yields the series of smooth shells $(X_K)_{K \in \mathbb{N}}$ with the coordinate functions $X_K := S_K^X X$. Note, that in practice we choose a sigmoid weight threshold and again truncate the series of projections in the shell operator (6) for indexes k where the weights are smaller. In our implementation we always use the threshold 0.01 for this purpose.

4.2 Step 1: Functional correspondences for Shells

One important choice for a shape registration pipeline is the representation and computation of correspondences. A straightforward way is to compute the point-to-point map $\mathbf{P} : \hat{X} \rightarrow \mathcal{Y}$ using a nearest neighbor search in some appropriate embedding space. However, these correspondences may not be accurate or meaningful when the surfaces are not perfectly aligned. Therefore, it is crucial to account for mismatched and noisy correspondences, otherwise errors tend to accumulate after a few iterations.

Functional Maps. We choose Functional Maps with an area preservation constraint and descriptor similarity assumption as explained in Section 3.3 for our pipeline. The overall objective for $\mathbf{C}^{(t)}$ with $K = K^{(t)}$ is the following.

$$\mathbf{C}^{(t)} = \arg \min_{\mathbf{C}^T \mathbf{C} = \mathbf{I}} \|\Psi_K \mathbf{C} - \mathbf{P}^{(t)} \Phi_K\|_{\mathbb{F}}^2 + \lambda_{\text{feat}} \|\mathbf{C} \Phi_K^T F^X - \Psi_K^T F^Y\|_{\mathbb{F}}^2. \quad (7)$$

In this context, we denote Φ_K and Ψ_K as the matrices of the first K stacked eigenfunctions of Δ^X and Δ^Y . $F^X \in \mathbb{R}^{N \times N_{\text{feat}}}$ and $F^Y \in \mathbb{R}^{M \times N_{\text{feat}}}$ are dense features on the surface. In general we can use different types of information and concatenate them in the feature vector. For example, the descriptors can come directly from the shells or from the original shapes X and Y . In our experiments we decided to use the latter, because a high level of detail improves the accuracy of descriptors like SHOT [47]. Moreover, they do not need to be recomputed in every iteration.

Functional maps are in some sense the optimal way to represent correspondences for our registration pipeline. In general, the pointwise adjacency matrix $\mathbf{P} \in \{0, 1\}^{N \times M}$ contains as many correspondences as there are points on the discretized surface. On the other hand, the compressed smooth shells (6) only have $3K$ degrees of freedom where $K \ll N$ which means that \mathbf{P} is subject to a lot of redundancy. Therefore, all we need to establish the relationship between the shells X_K and Y_K is a mapping between the eigenfunctions ϕ_1, \dots, ϕ_K and ψ_1, \dots, ψ_K , which is exactly the Functional Map \mathbf{C} .

We would like to support this claim by illustrating through the following example. Assume that X and Y are exactly isometric. Then we know that $\phi_k = \psi_k$ (normalized for sign flips) because the Laplacian is the same on both surfaces. In other words, the Functional Map \mathbf{C} in this case is just the identity \mathbf{I} . Using this knowledge then leads us to the following closed form expression for the exact alignment of

\mathcal{X}_K and \mathcal{Y}_K .

$$Y_K - X_K = S_K Y - S_K X = \sum_{k=1}^{\infty} \frac{1}{1 + \exp(\sigma(k-K))} \langle \phi_k, Y - X \rangle \phi_k. \quad (8)$$

Of course we do not have exact isometry in practice, but if we are able to determine the functional correspondences \mathbf{C} , we have a good approximation of the relationship between the two eigenbases $\mathbf{C}\phi_k \approx \psi_k$. Therefore a truncated Functional Map contains sufficient information to compute an alignment between two shells.

Pointwise Correspondence. For the optimization in the alignment step (Section 4.3) and the computation of the Functional Map in the next iteration an actual pointwise correspondence is needed. Converting a Functional Map to a pointwise correspondence is a problem in itself and we choose an extension of the spectral alignment proposed in the original paper (see part (c)) [32]. For this purpose we embed the shells $\hat{\mathcal{X}}_K$ and \mathcal{Y}_K from iteration $K = K^{(t)}$ in the $K+6$ dimensional product space of (a) their coordinates \hat{X}_K and Y_K , (b) their outer normals \hat{v}_K^X and v_K^Y and (c) the current spectral embedding using the following embedding functions:

$$\mathcal{E}_K^X : p \mapsto (\hat{X}_K(p), \lambda_{\text{norm}} \hat{v}_K^X(p), \lambda_{\text{spec}} \Phi_K(p)). \quad (9a)$$

$$\mathcal{E}_K^Y : q \mapsto (Y_K(q), \lambda_{\text{norm}} v_K^Y(q), \lambda_{\text{spec}} \Psi_K(q) \mathbf{C}). \quad (9b)$$

We find the pointwise correspondence by doing Euclidean nearest neighbor in this $K+6$ dimensional embedding space. Using extrinsic coordinates and outer normals improves the accuracy over [32] without much computational overhead.

4.3 Step 2: Shell Alignment

In every iteration we can use the pointwise correspondence from the last section to get a refined alignment. We parametrize the deformation of X with parameters $\tau \in \mathbb{R}^{K \times 3}$ such that $\hat{X}_K = X_K + \sum_{k=1}^K \tau_k \phi_k \approx Y_K$. A naive approach to this would be to directly shift each point $X_K(p)$ to their corresponding destination $Y_K(\mathbf{P}^{(t)}(p))$, but we add additional assumptions to make the overall mapping more realistic.

$$E_{\text{align}} := E_{\text{match}} + \lambda_{\text{arap}} E_{\text{arap}}. \quad (10)$$

First, we add an as-rigid-as-possible regularization term to the alignment which leads to shifts that locally resemble rigid transformations. The second assumption we make is based on the observation that just like for the geometry we can constrain the degrees of freedom of shell morphings to $3K$ in a low rank manner.

4.3.1 Matching Term. The matching term minimizes the Euclidean distances between the points \hat{X}_K and their current estimated destination $Y_K \circ \mathbf{P}^{(t)}$ under the assumption that the overall morphing can be represented with the spectral low-rank coefficients $\tau_k^{(t)}$.

$$E_{\text{match}}(\tau_1^{(t)}, \dots, \tau_K^{(t)}) := \left\| X_K + \sum_{k=1}^K \tau_k^{(t)} \phi_k - (Y_K \circ \mathbf{P}^{(t)}) \right\|^2 \quad (11)$$

The main motivation behind this is indicated in the example from Equation (8). The morphed shell $\hat{\mathcal{X}}_K$ and the reference shell \mathcal{Y}_K are represented in two different low rank bases, but the Functional Map we computed in the first step provides us with an approximate

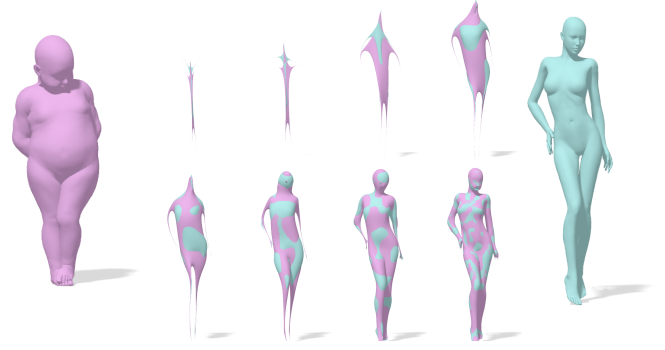


Fig. 4. Example of how the shells are aligned over the iterations. In the first iterations the alignment is still rough due to the restricted degrees of freedom in the deformation parameters but shape and pose are nearly identical in the end.

mapping $\mathbf{C}^{(t)}\phi_k \approx \psi_k$ between them.

$$\begin{aligned} \hat{X}_K &= X_K + \hat{X}_K - X_K = X_K + \mathcal{T}_K^X (\hat{X}_K - X_K) = \\ &= X_K + \underbrace{\sum_{k=1}^K \langle \hat{X}_K - X_K, \phi_k \rangle \phi_k}_{\tau_k^{(t)}} \approx Y_K \circ \mathbf{P}^{(t)} \end{aligned} \quad (12)$$

In the isometric setup from Equation (8) we have $\mathbf{C}^{(t)} = \mathbf{I}$ which means that we can compute an exact alignment for appropriate coefficients $\tau_k^{(t)}$. In the more general case, we can still get a sufficiently precise alignment with this strategy but we need significantly fewer degrees of freedom. This problem is well constrained and small deviations in the first iterations are not problematic. More importantly, for higher $K^{(t)} \geq 100$ the identity $\mathbf{C}^{(t)}\phi_k \approx \psi_k$ becomes close to exact and the quality of the alignment improves. Equation (12) induces the $3K$ -dimensional affine shape space of shells $\hat{\mathcal{X}}_K$ for arbitrary shifting coefficients $\tau_1^{(t)}, \dots, \tau_K^{(t)} \in \mathbb{R}^3$. This restriction also implicitly regularizes the shell morphings and removes outliers because of the natural low to high frequency ordering of the eigenfunctions ϕ_k .

4.3.2 As-Rigid-As-Possible Term. The second term is an as-rigid-as-possible (ARAP) regularization term which helps to preserve details and counteract distortions.

$$\begin{aligned} E_{\text{arap}}(\tau_1^{(t)}, \dots, \tau_K^{(t)}, R^{(t)}) := \\ \int_{\mathcal{N}_K(p)} \left\| (R^{(t)}(p) - \mathbf{I})(X(p) - X(q)) \right. \\ \left. - \sum_{k=1}^K \tau_k^{(t)} (\phi_k(p) - \phi_k(q)) \right\|_2^2 dq dp. \end{aligned} \quad (13)$$

This idea is quite common and prefers morphings that locally resemble a rigid transformation. For this purpose we determine the displacements parameterized by $\tau_k^{(t)}$ and a matrix $R^{(t)}(p) \in SO(3)$ for each vertex $p \in \mathcal{X}_K$, where $SO(3)$ is the Lie group of 3D rotation matrices. The objective demands that in a neighborhood $\mathcal{N}_K(p) \subset \hat{\mathcal{X}}_K$ of p the overall transformation should be approximately rigid. In our implementation we use the first degree neighborhood $\mathcal{N}_K(p)$ of each vertex $p \in \hat{\mathcal{X}}_K$ when interpreting the shape meshing as a graph.

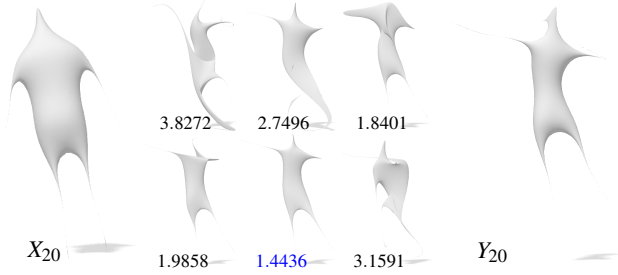


Fig. 5. Example of surrogate alignments in the initialization. X_{20} is shown on the right and Y_{20} on the left. In the middle is a subset of six deformations of X_{20} that are rated by the matching objective defined in Eq. 11. The blue one has the lowest energy and will therefore be used as initialization.

4.3.3 Optimization. We use a Gauss-Newton type optimization method to jointly compute the optimal shifting parameters $\tau_1^{(t)}, \dots, \tau_K^{(t)}$ and rotations $R^{(t)} : \mathcal{X}_K \rightarrow SO(3)$. In our experiments one update step per iteration t was sufficient when initializing $R^{(t)}$ and $\tau_k^{(t)}$ with the values from the previous iteration $t - 1$. Intuitively, in the beginning a rough alignment is sufficient because the space of admissible morphings is constrained to a low dimensional space and the coarse shells do not have distracting fine scale details. For higher order iterations the shells only minimally vary between $t - 1$ and t , and therefore the transformation parameters $\tau_k^{(t-1)}$ are a good initialization and close to the optimum. See Figure 3 for an example of how the alignment evolves.

After the last iteration we apply the morphing parameters from $\mathcal{X}_{K^{(T)}}$ to the original shape X get the final registration of the surfaces.

$$\hat{X}(p) := X(p) + \hat{X}_{K_{\max}}(p) - X_{K_{\max}}(p) \approx Y(\mathbf{P}^{(T)}(p)). \quad (14)$$

This morphed shape \hat{X} , the functional map $\mathbf{C} := \mathbf{C}^{(T)}$ and pointwise matchings $\mathbf{P} := \mathbf{P}^{(T)}$ constitute the output of our method.

5 INITIALIZATION: SURROGATE BASED MARKOV CHAIN MONTE CARLO SAMPLING

For any registration pipeline, the appropriate initial alignment is crucial to avoid getting stuck in nonmeaningful local minima. However, this first step is far from being trivial, especially in the presence of intrinsic symmetries and other self similarities which occur frequently in real world and synthetic shapes. The main problem is that neither the high level details nor the coarse features of e.g. a human shape are suitable to distinguish between the two legs or arms, especially if the details at the hands are noisy like in real scans. However, as humans we are usually still able to differentiate between left and right because we incorporate an additional piece of information: context. If the arms themselves are not sufficiently detailed, we can additionally look at their orientation and positioning at the whole body to determine which one is the right and left one.

Surrogate runs. We incorporate this idea into our pipeline by starting test runs with different deformations and rating their plausibility with the matching objective from Eq. (11).

The test runs are faster versions of the full pipeline but already stopping after \mathcal{X}_{20} and on shapes that were downsampled to 1000

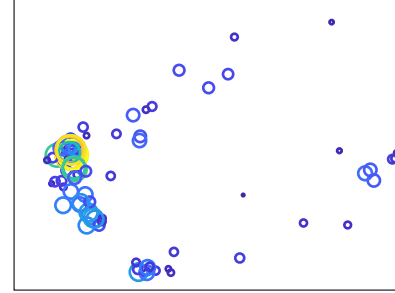


Fig. 6. The plot above shows the distribution of all surrogate results in our MCMC algorithm for the example in Figure 5. Each circle represents one vector with the deformation parameters $\tau_{20} \in \mathbb{R}^{60}$. The τ_{20} are embedded into 2D with Multidimensional Scaling to be visualizable. During the MCMC we sample 100 proposal deformations $\tau_6 \sim \mathcal{N}(0, \mathbf{I})$ and for each we perform a surrogate run to get $\tau_{20} := \text{Surr}(\tau_6)$. The negative log likelihood of each sample is the objective value $E_{\text{match}}(\tau_{20})$ that measures the alignment quality (see Figure 5). In the plot, higher likelihoods are displayed with bigger, yellow circles and smaller ones with small, blue circles. The cluster on the left side corresponds to the optimal initial alignment. This cluster emerges because the surrogate runs optimize for a good objective value.

vertices with Euclidean farthest point sampling. Moreover, we turn off the ARAP regularization $\lambda_{\text{arap}} = 0$ because for coarse shells with few degrees of freedom the problems are anyway well constrained. This version is significantly faster and less accurate but still sufficient to find the initial deformation for the full pipeline. See Figure 5 for example surrogate runs and how they are rated by the matching objective.

MCMC initialization. One of the main advantages of using our shells is that they admit a compact representation with only very few parameters. This simplifies the issue of creating proposal $\hat{\mathcal{X}}_K$ because we only have to consider the $3K^{(0)}$ dimensional space of potential shells. This furthermore allows us to define a prior distribution over the space of initial shells as the pushforward of a standard normal distribution over the shell parameters $\tau^{(0)} \sim \mathcal{N}(0, \mathbf{I})$. Furthermore, using the resulting alignments at $K^{(t)} = 20$ we can interpret the alignment energy (11) as the negative log likelihood of $\tau^{(0)}$. Using this, we can apply a Markov chain Monte Carlo (MCMC) Independence sampling algorithm to sample from the posterior distribution over $\tau^{(0)}$. Note, that a higher posterior density value is equivalent to a more faithful surrogate alignment and therefore a better initialization.

ALGORITHM 1. (MCMC)

1. Initialize $\tau_6^{(0)} := 0, \tau_{20}^{(0)} := 0$.
2. For $i = 1, \dots, 100$:
 - 2.1 Sample new proposal $\tau_6 \sim \mathcal{N}(0, \mathbf{I})$.
 - 2.2 Perform surrogate run $\tau_{20} := \text{Surr}(\tau_6)$.
 - 2.3 Compute the acceptance probability $\alpha(\tau_6, \tau_6^{(0)}) := \exp\left(-\frac{1}{2\sigma_{\text{match}}^2} (E_{\text{match}}(\tau_{20}) - E_{\text{match}}(\tau_{20}^{(0)}))\right)$.
 - 2.4 Sample $u \sim \text{Unif}(0, 1)$, update
$$(\tau_6^{(0)}, \tau_{20}^{(0)}) := \begin{cases} (\tau_6, \tau_{20}), & u \leq \alpha(\tau_6, \tau_6^{(0)}) \\ (\tau_6^{(0)}, \tau_{20}^{(0)}), & \text{otherwise} \end{cases}$$

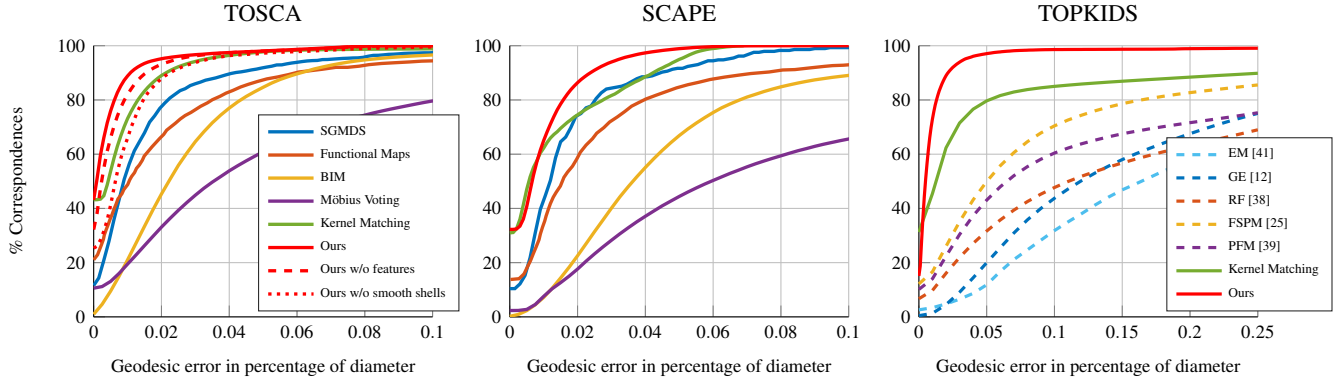


Fig. 7. The Figures above show our point-to-point matching accuracies for TOSCA [10], SCAPE [5] and TOPKIDS [21]. The curves show the percentage of matchings that have a geodesic error below a given threshold. On the first two datasets we compare our method against Spectral Generalized Multi-Dimensional Scaling (SGMDS) [2], Functional Maps [32], Blended Intrinsic Maps (BIM) [19], Möbius Voting [24] and Kernel Matching [50]. On TOPKIDS we on one hand compare against the methods mentioned in the original paper (Isometric Embedding via Expectation-Maximization (IE-EM) [41], Green’s Function Embedding Alignment (GFE) [12], Random Forests (RF) [38]), Fully Spectral Partial Matching (FSPM) [25], Partial Functional Maps (PFM) [39] and also add a comparison with the Kernel Matching (KM) [50] method. On TOSCA we additionally test our pipeline without any descriptors to show that it still provides highly accurate correspondences when it only acts on the 3D coordinates. Furthermore, we test it for the truncation operator \mathcal{T} to prove that our smooth shells are more suitable for iterative alignment than the naive approach.

In this context, we choose a small objective variance $\sigma_{\text{match}}^2 := 0.001$ to get a sharp distribution and therefore more accurate samples $\tau_6^{(0)}$. Our overall initialization strategy can be summarized as follows. At first, we compute a rigid alignment of the two input shapes with a feature based ICP algorithm. Then we apply Algorithm 1 to determine an appropriate alignment $\tau^{(0)} := \tau_6^{(0)}$ of the initial shells $K^{(0)} = 6$ which we then use to initialize the final registration run of our pipeline. See Figure 6 for an illustration of how Algorithm 1 works.

6 EXPERIMENTS

We perform various evaluations highlighting the flexibility of our method. First, we evaluate the correspondence accuracy on several benchmarks where our method outperforms other current shape matching methods. Secondly, we show that our method can be applied to a range of registration tasks for which we provide qualitative evaluations. This also includes non isometric shapes, either due to different topology or as an interclass matching problem. We use the same set of hyperparameters in all our experiments: $\lambda_{\text{feat}} = 20$, $\lambda_{\text{arap}} = 0.02$, $\lambda_{\text{norm}} = 0.04$, $\lambda_{\text{spec}} = 0.11$ and $\sigma := 0.5$ which we determined empirically. Furthermore, we choose a maximum of $K_{\text{max}} = 500$ eigenfunctions which constitutes a reasonable trade-off between complexity and accuracy. We use a logarithmic scale between $K^{(0)} = 6$ and $K^{(T)} = K_{\text{max}}$ because the changes between the shells tend to be higher for small K . The choice of $K^{(0)} = 6$ seems to work best as a starting point for our initialization strategy, see Section 5 for more details. For the descriptors in (7) we use the SHOT [47] and HKS [44] descriptors.

6.1 Point-to-point correspondences

We evaluate the matching accuracy of our method on the TOSCA [10], SCAPE [5], TOPKIDS [21] and SHREC’19 connectivity [29].

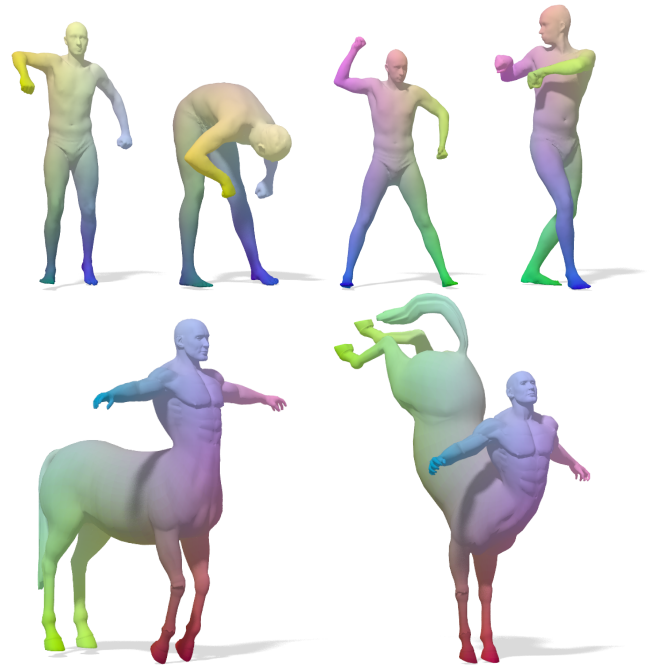


Fig. 8. Example matchings from the SCAPE and TOSCA dataset. Despite intrinsic symmetries and challenging poses our algorithm faithfully aligns the coarse features like the limbs of a human.

All these datasets have known ground truth correspondences. TOSCA consists of 76 shapes from 8 classes of humans and animals, in SCAPE there are 72 poses of the same person, TOPKIDS contains 25 poses of a human child and SHREC’19 connectivity has 44 shapes of different humans. All our experiments are performed according



Fig. 9. Example matchings from the TOPKIDS [21] (top) and SHREC'19 connectivity [29] (bottom) dataset. In TOPKIDS the meshes connect at self intersections which poses a problem for methods that assume near isometry. In SHREC'19 connectivity many input pairs have non compatible meshings with sampling sizes N, M varying from $5k$ to $200k$. This also means that there is no bijective point-to-point mapping, very often multiple vertices from \mathcal{X} need to be mapped to the same vertex one on the reference shape \mathcal{Y} .

to the Princeton benchmark protocol [19] which display the percentage of correspondences where the geodesic error surpasses certain thresholds, a perfect matching results in a constant curve at 100%.

$$\varepsilon(x) = \frac{d_{\mathcal{Y}}^{\text{Geo}}(y, y^*)}{\sqrt{\text{area}(\mathcal{Y})}}$$

See Figure 7 and Figure 11 for our results, as well as comparisons to other matching methods. We use the same setup of our method for all experiments. However, on TOSCA we additionally evaluate our pipeline without using any descriptors ($\lambda_{\text{feat}} = 0$). In general, we choose to keep the descriptors as they improve the accuracy in complicated settings. Figure 8 shows example matchings from SCAPE and TOSCA and Figure 9 from TOPKIDS and Connectivity. We also evaluate the necessity of the smooth shells to our framework and show how the same algorithm performs with spectral reconstruction instead of smooth shells. The results are shown in Figure 7. Many examples fail due to major changes between consecutive iterations and the mistakes accumulate until the end.

TOSCA and SCAPE contain shapes with consistent meshing within each class. The shapes in TOPKIDS are synthetic but at self intersections the shapes were reduced to the outer hull which causes topological changes in the meshes similar to real scans. The main assumption for our method is that the two input shapes have the same coarse structure but they do not need to be isometric, therefore, the effect of topological changes is not as severe and we outperform other methods that rely on near isometry. The SHREC'19 Connectivity dataset focusses on pairs of human shapes from different classes and with serve differences in the meshing, ranging from template sized shapes ($N \approx 5000$ vertices) to real scans ($>200K$ vertices). Again we outperform all competing methods as the Functional Map representation is independent of the sampling density but the alignment



Fig. 10. Example matchings from the FAUST [6] dataset which contains scans from real humans. The shapes displayed here are very high resolution (200k vertices) and subject to noise and topological changes. The example on the right is especially challenging due to huge partiality and cannot be handled by many methods. Our correspondence is still meaningful although there are some discontinuities due to the partiality.

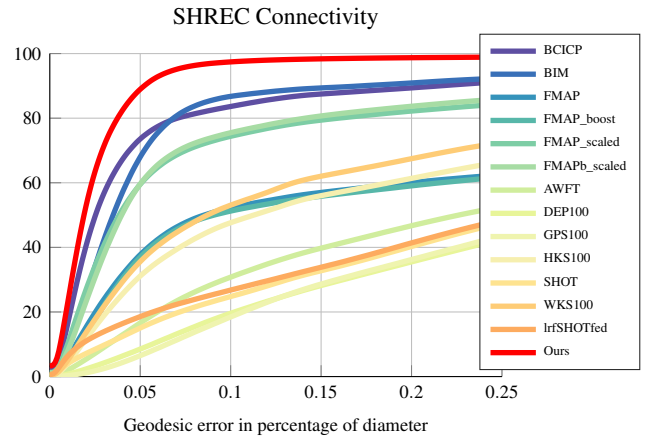


Fig. 11. Our matching results for the SHREC'19 [29] connectivity challenge. The dataset contains 430 pairs of human shapes in different poses where many pairs have a different sampling size and meshing. In the extreme case templates are matched to real high resolution scans with $N \approx 5k$ and $M \approx 200k$.

strategy is flexible enough to deal with non-isometries. Notice that our pipeline did not need any adaptations to deal with the different challenges in the datasets.

6.2 Qualitative Experiments

In this section, we show examples of surface alignment and correspondence between pairs for which no ground-truth correspondence exists. Since the examples are interclass they are in general more challenging but we are still able to show visually convincing results. In Figure 12 we show some matching results for different challenging interclass correspondences that are even beyond different human body shapes. The Faust Scan dataset [6] contains real scans of different humans in multiple poses with up to 200k vertices. Since the scans are real they contain scanning noise, holes and topological merges. Additionally, no ground-truth exists but we show qualitative



Fig. 12. Matching results for interclass examples. The pair in the top left is the example from the teaser, the top right is the particularly challenging pair human and horse. In the bottom we show a morphing from a human template from FAUST [6] to a real scan of a statue [1].

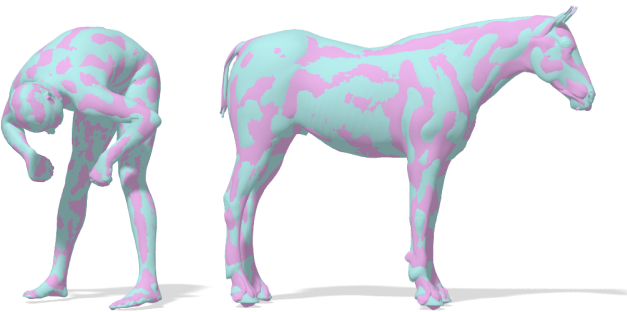


Fig. 13. Overlays of the final alignments of a SCAPE intraclass pair (left) and the dog and horse pair (right) as also shown in Figure 1.

results in Figure 10. In Figure 13 we show the overlap of the final alignments of a SCAPE pair and the dog and horse pair.

6.3 Correspondence Recovery from Functional Maps

Our registration method uses Functional Maps to represent correspondences between two surfaces. In this context, we propose (9) to recover pointwise matchings by performing a nearest neighbor search in the product space of the spectral coefficients, outer normals and Euclidean coordinates. This goes beyond the standard Functional Maps methodology where only the spectral coefficients are used. An important question in this context is how much our method depends on the quality of the Functional Maps it uses. We use a combination

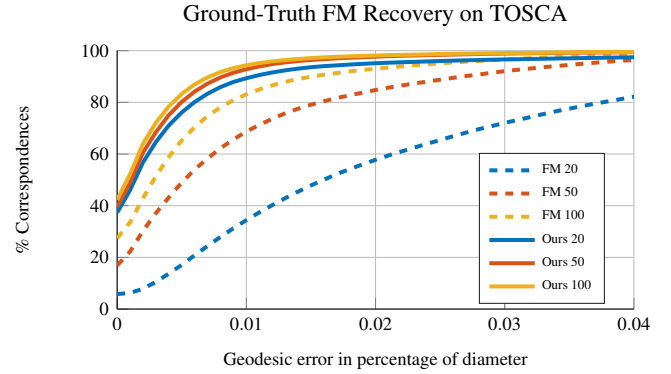


Fig. 14. Results of pointwise Functional Map recovery experiments on TOSCA. We compare ourselves with the standard spectral nearest neighbor approach from the Functional Maps paper [32]. Our method uses the domain knowledge about shapes to recover highly accurate correspondences, even if the input maps \mathbf{C} are small. From 50x50 to 100x100 maps the input does not vary much which although more ground truth information is available. This is an indication that at this stage of the alignment our algorithm profits already to a high degree from the coarser alignments and therefore corrections with additional information are not as beneficial as in early stages.

of descriptors and the current shell alignment to compute a Functional Map in each iteration. Both of those are prone to noise, especially in the beginning when the shell alignment is rough. To investigate this dependency we test our pipeline using different precomputed Functional Maps instead of computing \mathbf{C} in the algorithm. Like this our method can be used to recover the point-to-point correspondences $\mathbf{P} \in \mathbb{R}^{N \times N}$ from the compressed representation $\mathbf{C} \in \mathbb{R}^{K \times K}$. The recovery step is crucial in any Functional Maps pipeline. If it is done improperly, it can lead to a significant decrease in accuracy and add noise which limits the applicability of the matchings.

For the evaluations presented here we incorporate a sparse set of N_{gt} ground truth correspondences and use them to construct a Functional Map according to Equation (4). This should simulate how our method can be used to recover dense correspondence by using the sparse output of another matching pipeline. We use different basis sizes $K \in \{20, 50, 100\}$ and sampled points $N_{\text{gt}} \in \{100, 200, 500\}$ and compare our method against the spectral nearest neighbor recovery proposed in the Functional Maps paper [32], see Figure 14. Those results prove that our point-to-point recoveries are more accurate than the standard method, especially for small input sizes K . Additionally, our method does not improve much as the size of the input Functional Map grows. This is surprising because for higher K the Functional Map includes a lot more high frequency information. This indicates that at this stage our method is able to determine faithful estimates for the higher order Functional Maps with just using the alignments from the previous steps.

6.4 Runtime analysis

In terms of runtime complexity, our method can be decomposed in three parts with approximately the same magnitude: Computation of the features (500 eigenpairs of \mathcal{X} and \mathcal{Y} and the SHOT [47] and HKS [44] descriptors), the initial pose estimation (rigid alignment and

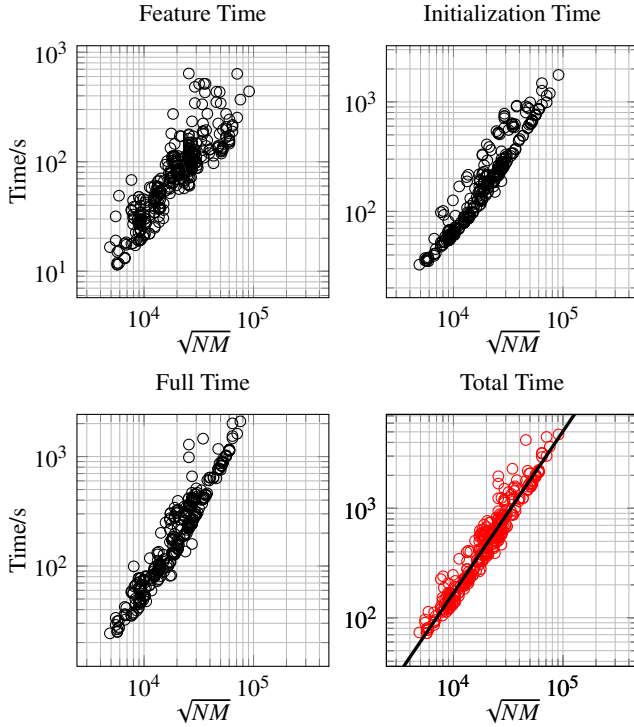


Fig. 15. Runtime analysis of our pipeline on the SHREC'19 dataset. The average runtime is 663 seconds with a high variance because the mesh sizes N and M vary a lot. The subfigures refer to the runtimes of (top left) the feature computation, (top right) the MCMC initialization step, (bottom left) the full alignment after initialization, (bottom right) the total runtime which is the sum of the three previous ones. The empirical dependency of the total computation time is $O(\sqrt{NM}^{1.47})$.

mainly the MCMC initialization) and the final alignment. In general the runtime mostly depends on the size of the input shapes N and M . The main computational overhead of the main alignment method is the computation of the as-rigid-as-possible regularizer (13) with a complexity $O(N)$ (for standard shapes with bounded neighborhood size) and the nearest neighbor computation for the pointwise recovery (9) in $O(NM)$. The MCMC initialization performs 100 surrogate runs with an average runtime of 0.46 seconds. Those evaluations are computed on subsampled shapes with 1000 vertices, therefore they are essentially independent of N and M . However, the evaluation of the matching energy (11) is performed on the full shapes with one nearest neighbor search, therefore the overall algorithm still depends on the sampling size of the inputs.

The SHREC'19 dataset focuses on shapes with different connectivity and therefore contains shape pairs with a large variety of sampling sizes N and M . See Figure 15 for a full empirical runtime analysis of our method on this dataset. Here, we evaluate the dependency of the runtimes on the aggregate of the shape sizes \sqrt{NM} which results in an average of 663 seconds. The noise in the plots comes from the fact that in general it makes a difference if the points have approximately the same number of vertices $N \approx M$ or if one of them is severely

#Subsamples	500	1000	2000	5000	10000	20000	All
Mean runtime	133.8	134.3	134.5	137.3	161.3	237.3	368.5
Mean error	0.0126	0.0090	0.0069	0.0057	0.0054	0.0049	0.0049

Fig. 16. Runtime analysis on TOSCA for the full run of the method for different subsampling sizes. A higher number of vertices increases the accuracy of the method but after a certain point it starts plateauing. For a subsampling of at most 20k vertices the results are indistinguishable from the full vertex size. On the other hand, the computational complexity increases significantly for more vertices which is a strong argument for using subsamplings in practice, especially for high resolution shapes where more points do not add significantly more information.

bigger than the other one. The empirical runtime complexity of our method on this dataset is around $O(\sqrt{NM}^{1.47})$. In other words, for shapes with $N = M$ the empirical complexity is $O(N^{1.47})$.

One thing we want to advocate in this context is that in general it can also make sense to use an a priori subsampling of the input shapes for the full run and not only for the surrogates. We refrain from doing it in our experiments because we want to achieve maximum accuracy but very often the additional information gained by using the full shapes is insignificant in comparison to the additional computational overhead, especially for high resolution shapes $N > 100k$. To investigate this we subsample the shapes from TOSCA with Euclidean farthest point sampling and compute the full run of our method for the different settings, see Figure 16. It turns out that in this case the accuracy starts plateauing at some point while the runtime increases significantly.

7 CONCLUSION

We presented a novel approach to shape registration that combines intrinsic information through Functional Maps and extrinsic information to calculate an alignment in the 3D embedding space. The framework introduces the notion of smooth shells to define a series of coarse-to-fine shape approximations with the property that consecutive shells $\mathcal{S}_K(X)$ and $\mathcal{S}_{K+1}(X)$ always have minimal offsets which is an advantage for iterative methods. Furthermore, we solve the problem of self-similarities by starting with a surrogate based Markov chain Monte Carlo approach in which the deformation energy is used to find the optimal initialization. Finally, we show state-of-the-art results on established isometry datasets as well as on two datasets which focus on specific noise, namely different meshing and topology changes. Notice that we outperform all methods on these two datasets without adapting our pipeline although the shapes in both are subject to completely different types of noise. Additionally, we show qualitative examples of interclass correspondences on challenging cases like human to horse.

In future work we would like to extend our framework to using more general morphing models like affine mappings. This might allow our method to work with less transformation basis functions. Furthermore, we would like to incorporate partial functional correspondences [39] to apply our framework to partial data.

REFERENCES

- [1] [n.d.]. Scan of Discobolus at the British Museum. <https://www.myminifactory.com/object/3d-print-discobolus-at-the-british-museum-london-7896>. Accessed: 2019-02-17.

- [2] Yonathan Aflalo, Anastasia Dubrovina, and Ron Kimmel. 2016. Spectral generalized multi-dimensional scaling. *IJCV* 118, 3 (2016), 380–392.
- [3] Ibraheem Alhashim, Kai Xu, Yixin Zhuang, Junjie Cao, Patricio Simari, and Hao Zhang. 2015. Deformation-driven Topology-varying 3D Shape Correspondence. *ACM Trans. Graph.* 34, 6, Article 236 (Oct. 2015), 13 pages.
- [4] Brian Amberg, Sami Romdhani, and Thomas Vetter. 2007. Optimal Step Nonrigid ICP Algorithms for Surface Registration. *Proc. of IEEE Conference on Computer Vision and Pattern Recognition (CVPR)* (2007).
- [5] Dragomir Anguelov, Praveen Srinivasan, Daphne Koller, Sebastian Thrun, Jim Rodgers, and James Davis. 2005. SCAPE: shape completion and animation of people. In *ACM transactions on graphics (TOG)*, Vol. 24. ACM, 408–416.
- [6] Federica Bogo, Javier Romero, Matthew Loper, and Michael J. Black. 2014. FAUST: Dataset and evaluation for 3D mesh registration. In *Proceedings IEEE Conf. on Computer Vision and Pattern Recognition (CVPR)*. IEEE, Piscataway, NJ, USA.
- [7] Federica Bogo, Javier Romero, Gerard Pons-Moll, and Michael J. Black. 2017. Dynamic FAUST: Registering Human Bodies in Motion. In *IEEE Conf. on Computer Vision and Pattern Recognition (CVPR)*.
- [8] Mario Botsch and Olga Sorkine. 2007. On linear variational surface deformation methods. *IEEE transactions on visualization and computer graphics* 14, 1 (2007), 213–230.
- [9] Mario Botsch, Robert Sumner, Mark Pauly, and Markus Gross. 2006. Deformation transfer for detail-preserving surface editing. In *Vision, Modeling & Visualization*. Citeseer, 357–364.
- [10] Alexander M Bronstein, Michael M Bronstein, and Ron Kimmel. 2008. *Numerical geometry of non-rigid shapes*. Springer. http://tosca.cs.technion.ac.il/book/resources_data.html.
- [11] Alexander M. Bronstein, Michael M. Bronstein, and Ron Kimmel. 2009. Topology-Invariant Similarity of Nonrigid Shapes. *International Journal of Computer Vision* 81 (2009), 281–301. <https://doi.org/10.1007/s11263-008-0172-2>
- [12] Oliver Burghard, Alexander Dieckmann, and Reinhard Klein. 2017. Embedding Shapes with Green’s functions for Global Shape Matching. *Computers & Graphics* 68C (2017), 1–10.
- [13] Junjie Cao, Andrea Tagliasacchi, Matt Olson, Hao Zhang, and Zhinxun Su. 2010. Point Cloud Skeletons via Laplacian Based Contraction. In *Proceedings of the 2010 Shape Modeling International Conference (Shape Modeling International Conference (SMI) 2010)*. IEEE Computer Society, Washington, DC, USA, 187–197. <https://doi.org/10.1109/SMI.2010.25>
- [14] Etienne Corman, Justin Solomon, Mirela Ben-Chen, Leonidas Guibas, and Maks Ovsjanikov. 2017. Functional Characterization of Intrinsic and Extrinsic Geometry. *ACM Trans. Graph.* 36, 2 (March 2017). <https://doi.org/10.1145/2999535>
- [15] M. Eisenberger, Z. Löhner, and D. Cremers. 2018. Divergence-Free Shape Interpolation and Correspondence. In *arXiv:1806.10417*.
- [16] Danielle Ezuz and Mirela Ben-Chen. 2017. Deblurring and Denoising of Maps between Shapes. *Computer Graphics Forum (CGF)* 36, 5 (August 2017).
- [17] Thibault Groueix, Matthew Fisher, Vladimir G. Kim, Bryan C. Russell, and Mathieu Aubry. 2018. 3D-CODED: 3D Correspondences by Deep Deformation. In *The European Conference on Computer Vision (ECCV)*.
- [18] Igor Guskov, Wim Sweldens, and Peter Schröder. 1999. Multiresolution signal processing for meshes. In *Proceedings of the 26th annual conference on Computer graphics and interactive techniques*. Citeseer, 325–334.
- [19] Vladimir G. Kim, Yaron Lipman, and Thomas A. Funkhouser. 2011. Blended intrinsic maps. *Trans. Graphics* 30, 4 (2011).
- [20] Leif Kobbelt, Swen Campagna, Jens Vorsatz, and Hans-Peter Seidel. 1998. Interactive multi-resolution modeling on arbitrary meshes. In *Siggraph*, Vol. 98. 105–114.
- [21] Z Löhner, Emanuele Rodolà, MM Bronstein, Daniel Cremers, Oliver Burghard, Luca Cosmo, Andreas Dieckmann, Reinhard Klein, and Y Sahillioglu. 2016. SHREC’16: Matching of deformable shapes with topological noise. *Proceedings of Eurographics Workshop on 3D Object Retrieval (3DOR)* 2 (2016), 11.
- [22] Bruno Lévy and Hao Richard Zhang. 2010. Spectral mesh processing. In *ACM SIGGRAPH 2010 Courses*. ACM, 8.
- [23] Hao Li, Robert W Sumner, and Mark Pauly. 2008. Global correspondence optimization for non-rigid registration of depth scans. In *Computer graphics forum*, Vol. 27. Wiley Online Library, 1421–1430.
- [24] Yaron Lipman and Thomas Funkhouser. 2009. Möbius voting for surface correspondence. In *Trans. Graphics*, Vol. 28. 72.
- [25] Or Litany, Emanuele Rodolà, Alex Bronstein, and Michael Bronstein. 2017. Fully Spectral Partial Shape Matching. *Computer Graphics Forum* 36, 2 (2017), 1681–1707.
- [26] Or Litany, Emanuele Rodolà, Alex M. Bronstein, Michael M. Bronstein, and Daniel Cremers. 2016. Non-Rigid Puzzles. *Computer Graphics Forum (CGF), Proceedings of Symposium on Geometry Processing (SGP)* 35, 5 (2016).
- [27] Jiayi Ma, Ji Zhao, Jinwen Tian, Alan L Yuille, and Zhuowen Tu. 2014. Robust point matching via vector field consensus. *IEEE Transactions on Image Processing* 23, 4 (2014), 1706–1721.
- [28] Riccardo Marin, Simone Melzi, Emanuele Rodola, and Umberto Castellani. 2018. FARM: Functional Automatic Registration Method for 3D Human Bodies. *CoRR* abs/1807.10517 (2018). <http://arxiv.org/abs/1807.10517>
- [29] Simone Melzi, Riccardo Marin, Emanuele Rodolà, and Umberto Castellani. 2019. Matching Humans with Different Connectivity. *Proceedings of Eurographics Workshop on 3D Object Retrieval (3DOR)* (2019).
- [30] Andriy Myronenko and Xubo Song. 2010. Point Set Registration: Coherent Point Drift. *IEEE Transactions on Pattern Analysis and Machine Intelligence* 32, 12 (2010), 2262–2275.
- [31] D. Nogneng, S. Melzi, E. Rodolà, U. Castellani, M. Bronstein, and M. Ovsjanikov. 2018. Improved Functional Mappings via Product Preservation. *Computer Graphics Forum (CGF)* 37, 2 (May 2018).
- [32] Maks Ovsjanikov, Mirela Ben-Chen, Justin Solomon, Adrian Butscher, and Leonidas Guibas. 2012. Functional maps: a flexible representation of maps between shapes. *ACM Transactions on Graphics (TOG)* 31, 4 (2012), 30.
- [33] Beresford N Parlett. 1998. *The symmetric eigenvalue problem*. Vol. 20. siam.
- [34] Ulrich Pinkall and Konrad Polthier. 1993. Computing Discrete Minimal Surfaces and Their Conjugates. *EXPERIMENTAL MATHEMATICS* 2 (1993), 15–36.
- [35] Gerard Pons-Moll, Javier Romero, Naureen Mahmood, and Michael J. Black. 2015. Dyna: A Model of Dynamic Human Shape in Motion. *ACM Transactions on Graphics, (Proc. SIGGRAPH)* 34, 4 (aug 2015), 120:1–120:14.
- [36] Jing Ren, Adrien Poulenard, Peter Wonka, and Maks Ovsjanikov. 2018. Continuous and Orientation-preserving Correspondences via Functional Maps. *ACM Trans. Graph.* 37, 6, Article 248 (Dec. 2018), 16 pages.
- [37] Dennie Reniers, Jarke van Wijk, and Alexandru Telea. 2008. Computing Multiscale Curve and Surface Skeletons of Genus 0 Shapes Using a Global Importance Measure. *IEEE Transactions on Visualization and Computer Graphics* 14, 2 (March 2008), 355–368. <https://doi.org/10.1109/TVCG.2008.23>
- [38] Emanuele Rodolà, Samuel Rota Bulò, Thomas Windheuser, Matthias Vestner, and Daniel Cremers. 2014. Dense non-rigid shape correspondence using random forests. In *Proc. CVPR*.
- [39] Emanuele Rodolà, Luca Cosmo, Michael Bronstein, Andrea Torsello, and Daniel Cremers. 2016. Partial Functional Correspondence. *Computer Graphics Forum (CGF)* (2016).
- [40] Emanuele Rodolà, Michael Moeller, and Daniel Cremers. 2015. Point-wise Map Recovery and Refinement from Functional Correspondence. In *Vision, Modeling and Visualization*. The Eurographics Association.
- [41] Yusuf Sahillioglu and Yücel Yemez. 2012. Minimum-Distortion Isometric Shape Correspondence Using EM Algorithm. *IEEE Trans. Pattern Anal. Mach. Intell.* 34, 11 (2012), 2203–2215.
- [42] Joaquim Salvi, Carles Matabosch, David Fofi, and Josep Forest. 2007. A Review of Recent Range Image Registration Methods with Accuracy Evaluation. *Image Vision Comput.* 25, 5 (2007), 578–596.
- [43] Robert W. Sumner, Johannes Schmid, and Mark Pauly. 2007. Embedded Deformation for Shape Manipulation. (2007). <https://doi.org/10.1145/1275808.1276478>
- [44] Jian Sun, Maks Ovsjanikov, and Leonidas Guibas. 2009. A concise and provably informative multi-scale signature based on heat diffusion. In *Computer graphics forum*, Vol. 28. Wiley Online Library, 1383–1392.
- [45] Andrea Tagliasacchi, Thomas Delame, Michaela Spagnuolo, Nina Amenta, and Alexandru Telea. 2016. 3D Skeletons: A State-of-the-Art Report. In *Computer Graphics Forum (CGF) (Proceedings of Eurographics)*, Vol. 35.
- [46] Gary K. L. Tam, Zhi-Quan Cheng, Yu-Kun Lai, Frank C. Langbein, Yonghuai Liu, David Marshall, Ralph R. Martin, Xian-Fang Sun, and Paul L. Rosin. 2013. Registration of 3D Point Clouds and Meshes: A Survey from Rigid to Nonrigid. *IEEE Transactions on Visualization and Computer Graphics* 19, 7 (July 2013), 1199–1217.
- [47] Federico Tombari, Samuele Salti, and Luigi Di Stefano. 2010. Unique signatures of histograms for local surface description. In *Proceedings ECCV* 16, 9 (2010), 356–369.
- [48] Bruno Vallet and Bruno Lévy. 2008. Spectral geometry processing with manifold harmonics. In *Computer Graphics Forum*, Vol. 27. Wiley Online Library, 251–260.
- [49] Oliver van Kaick, Hao Zhang, Ghassan Hamarneh, and Daniel Cohen-Or. 2011. A Survey on Shape Correspondence. *Computer Graphics Forum* 30, 6 (2011), 1681–1707.
- [50] Matthias Vestner, Zorah Löhner, Amit Boyarski, Or Litany, Ron Slossberg, Tal Remez, Emanuele Rodolà, Alex M. Bronstein, Michael M. Bronstein, Ron Kimmel, and Daniel Cremers. 2017. Efficient Deformable Shape Correspondence via Kernel Matching. In *International Conference on 3D Vision (3DV)*.
- [51] M. Vestner, R. Litman, E. Rodola, A. Bronstein, and D. Cremers. 2017. Product Manifold Filter: Non-Rigid Shape Correspondence via Kernel Density Estimation in the Product Space. In *IEEE Conference on Computer Vision and Pattern Recognition (CVPR)*.